

# Atomic Ordering-Induced Ensemble Variation in Alloys Governs Electrocatalyst On/Off States

Tianyao Gong, Guotao Qiu, Mo-Rigen He, Olga V. Safonova, Wei-Chang Yang, David Raciti, Corey Oses, and Anthony Shoji Hall\*



Cite This: *J. Am. Chem. Soc.* 2025, 147, 510–518



Read Online

ACCESS |

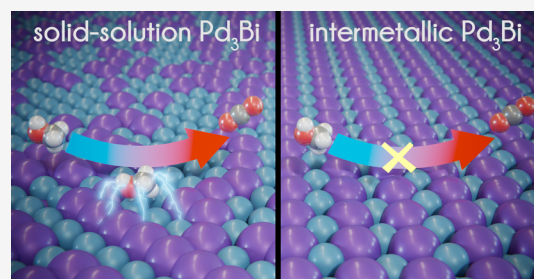
Metrics & More

Article Recommendations

Supporting Information

**ABSTRACT:** The catalytic behavior of a material is influenced by ensembles—the geometric configuration of atoms on the surface. In conventional material systems, ensemble effects and the electronic structure are coupled because these strategies focus on varying the material composition, making it difficult to understand the role of ensembles in isolation. This study introduces a methodology that separates geometric effects from the electronic structure. To tune the Pd ensemble size on the catalyst surface, we compared the reactivity of structurally different but compositionally identical Pd<sub>3</sub>Bi intermetallic and solid solution alloys. Pd<sub>3</sub>Bi intermetallics display no reactivity for methanol oxidation (MOR), while their solid solution counterparts show significant reactivity (0.5 mA cm<sub>Pd</sub><sup>-2</sup>).

Intermetallics form smaller ensembles (1, 3, 4, and 5 atoms across all low-energy facets), whereas solid solution Pd<sub>3</sub>Bi has several facets that support larger Pd ensembles, with an average size of 5.25 atoms and up to 6 atoms. A partially ordered Pd<sub>3</sub>Bi (a mixed phase of intermetallic and solid solution) alloy shows intermediate MOR activity (0.1 mA cm<sub>Pd</sub><sup>-2</sup>), confirming that methanol oxidation activity tracks with the average ensemble size. All Pd<sub>3</sub>Bi alloys maintained similar electronic structures, as confirmed by X-ray photoelectron spectroscopy (XPS) valence band spectroscopy and X-ray absorption near edge structure (XANES) measurements, indicating that reactivity differences arise from variations in the ensemble size induced by differences in the atomic ordering. Our findings offer an approach for designing materials with controllable active site configurations while maintaining the catalyst's electronic structure, thereby enabling more efficient catalyst design.



## INTRODUCTION

The escalating challenges of climate change and increasing global energy demands have intensified the need for clean and sustainable energy technologies. Electrocatalysis plays a crucial role in this energy transition, necessitating the need for innovative materials and strategies to efficiently mediate key reactions for renewable energy conversion and storage.<sup>1–6</sup> At the heart of these systems is the catalyst, which controls the rate of the reaction and selectivity of the process.<sup>7–12</sup> By manipulating the properties of the catalyst material, the reaction performance can be optimized.<sup>13–18</sup>

Bimetallic alloys, initially gaining prominence in heterogeneous catalysis in the 1960s, have risen to the forefront of electrocatalysis research.<sup>19</sup> The approach to understanding these materials focuses on analyzing variations in their electronic structure, particularly through the d-band center theory.<sup>16</sup> However, the complexity of catalyst design extends beyond the electronic structure of the material. Another important aspect in catalyst design is the ensembles.<sup>17,20–22</sup> These ensembles refer to clusters of specific atoms on the catalyst's surface, and their size—the number of atoms they contain—can have a significant impact on the reactivity. The ensembles comprise the active site of the catalyst and can

directly influence adsorption and activation of reactants by controlling the amount of surface atoms that interact with adsorbates. Moreover, controlling the configuration of ensembles can help overcome the limitations set by scaling relationships, providing an additional way to enhance catalytic performance that goes beyond just tweaking the electronic structure.<sup>23</sup>

The ensemble effect is typically assessed by varying the composition of solid solution alloys or surface alloys.<sup>24–27</sup> Increasing the proportion of the active element, M, in a bimetallic solid solution alloy (M–X), where X is a metal different than M, leads to a higher coordination number of M atoms among each other, thereby enlarging its ensemble size. However, adjusting an alloy's composition to examine ensemble size simultaneously impacts various properties: it not only changes the ensemble size but also the electronic

**Received:** August 26, 2024

**Revised:** December 4, 2024

**Accepted:** December 4, 2024

**Published:** December 23, 2024



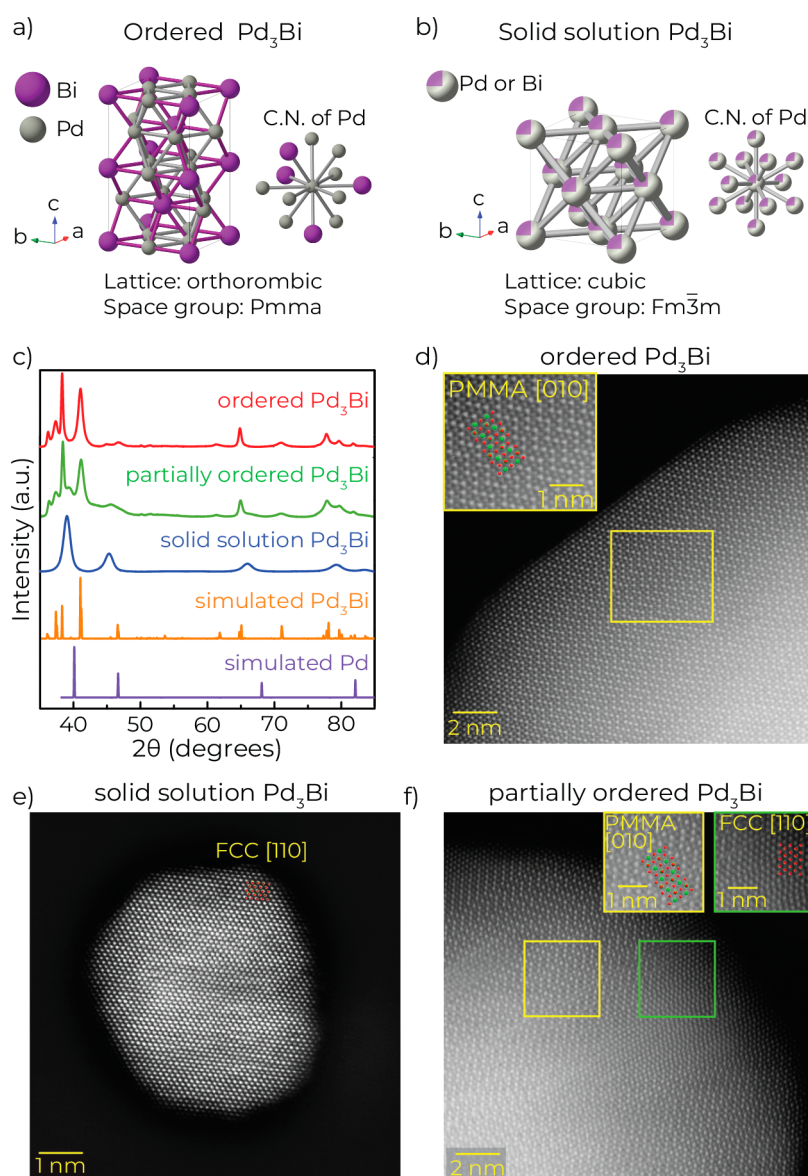


**Figure 1.** Unit cell and coordination environment of (a) ordered Pd<sub>3</sub>Bi and (b) solid solution Pd<sub>3</sub>Bi. (c) Powder X-ray diffraction (XRD) patterns of Pd<sub>3</sub>Bi with varying degrees of order. The simulated XRD patterns of Pd<sub>3</sub>Bi and Pd are from ICSD collection codes No. 58839 and No. 52251, respectively. High-angle annular dark-field scanning transmission electron microscopy (HAADF-STEM) images of (d) ordered, (e) solid solution, and (f) partially ordered Pd<sub>3</sub>Bi. The insets within panels (d–f) offer zoomed-in perspectives of particular areas, highlighted by the color of the surrounding boxes. Within these insets, an overlay of the ordered or solid solution Pd<sub>3</sub>Bi crystal is presented, aligned along the designated crystal direction. pmma is the space group for the ordered Pd<sub>3</sub>Bi which adopts an orthorhombic lattice, and FCC denotes face centered cubic crystal structure adopted by solid solution Pd<sub>3</sub>Bi. The TEM images in this figure are shown for samples collected after cyclic voltammetry and methanol oxidation.

structure.<sup>28,29</sup> This alteration in electronic structure results from shifts in the bond lengths, which vary with the lattice parameter of the solid solution, as well as from changes in electron density due to charge transfer between elements of different electronegativity (ligand effect).<sup>28,29</sup> The convolution of ensemble size with the electronic structure makes it difficult to isolate the role of ensembles, thereby hindering the development of more effective catalysts.

Intermetallic materials are a subclass of alloys in which each element has a fixed atomic position and site occupancy within the crystal, establishing long-range atomic ordering. These atomically precise structures enable one to create materials with controlled configurations of the active site on the surface (i.e., ensemble). This approach has been leveraged to create

materials with interesting catalytic reactivity. For example, a study showed that intermetallic Pd<sub>40</sub>Cu<sub>60</sub> system had high activity for the thermal semihydrogenation of acetylene to ethylene.<sup>30</sup> This study suggested that the intermetallic was more active than the solid solution Pd<sub>40</sub>Cu<sub>60</sub> because of partially isolated Pd active sites. Similarly, another study showed that substituting Zn sites with Pd in the  $\gamma$ -brass phase of a Pd–Zn intermetallic system allowed the tuning of Pd ensembles from monomers to trimers.<sup>22</sup> This methodology showed that Pd monomers were crucial for achieving improved selectivity for the semihydrogenation of acetylene. The use of intermetallics has also been extended to design efficient electrocatalysts. For example, intermetallic Pt<sub>3</sub>Ti was shown to be 4 times more active than solid solution Pt<sub>3</sub>Ti.<sup>31</sup> The strategy

of comparing intermetallic materials vs solid-solutions (often called random alloys) is a strategy that has been leveraged in electrocatalysis on various materials platforms.<sup>32–35</sup> These examples highlight the unique reactivity of intermetallic systems and their potential for precisely controlling the active-site geometry (ensemble size). However, it is important to note that most of these studies have not included experimental quantification of the electronic structures, a critical factor in verifying the independence of the ensemble changes within these systems from electronic structure changes. This observation highlights a significant research opportunity to investigate whether the strategy of adjusting atomic ordering—intermetallic versus random alloy—can facilitate independent control over ensemble size and electronic structure.

Herein, we investigated various Pd<sub>3</sub>Bi polymorphs to manipulate the ensemble size and determine its effect on catalytic efficiency. This approach allowed us to isolate the influence of the ensembles, as the fixed composition of the different polymorphs minimized changes to the electronic structure of the system while adjusting the ensemble size. Notably, our previous work indicated that Pd–Bi intermetallics were inactive for methanol oxidation, unlike other reports that suggested high activity for Pd–Bi alloys for various alcohol oxidations.<sup>10,36</sup> However, these other reports typically lacked detailed crystallographic characterization, leading us to assume that the materials discussed were likely solid solutions. This discrepancy led us to hypothesize that differences in crystalline structure might underlie the varied reactivity, prompting us to select the methanol oxidation reaction (MOR) as a probe reaction. We explored two polymorphs: ordered intermetallic Pd<sub>3</sub>Bi (henceforth denoted as ordered Pd<sub>3</sub>Bi) with a primitive orthorhombic crystal structure (*Pmma* space group) and solid solution Pd<sub>3</sub>Bi with a face-centered cubic structure (*Fm3m* space group).<sup>37</sup> Orthorhombic Pd<sub>3</sub>Bi, with its lower symmetry structure, exhibits a smaller average Pd–Pd coordination number within the bulk of the crystal. Specifically, in ordered Pd<sub>3</sub>Bi, the first coordination shell of Pd in the bulk of the crystal consists of a Pd atom surrounded by 8 Pd and 4 Bi atoms, resulting in a total coordination number (CN) of 12 (Figure 1a). In contrast, the face-centered cubic structure of solid solution Pd<sub>3</sub>Bi should statistically promote larger Pd–Pd coordination number in the bulk of the crystal due its random atomic arrangement. For solid solution Pd<sub>3</sub>Bi, each atom in the bulk of the FCC lattice has a CN of 12, with the statistical average CN being 9 for Pd–Pd and 3 for Pd–Bi, based on the composition (Figure 1b). Based on these variations of the crystal structure and atomic ordering in the bulk, we would expect the surfaces of these compositionally identical materials to display different ensemble sizes on the surface. Analysis of the Pd ensemble sizes on the surface indicated that intermetallic Pd<sub>3</sub>Bi has Pd–Pd cluster sizes of 1, 3, 4, or 5 atoms across all low-energy facets, whereas solid solution Pd<sub>3</sub>Bi has several facets that support larger Pd ensembles, with an average size of 5.25 atoms and up to 6 atoms. Therefore, solid-solution Pd<sub>3</sub>Bi displayed larger ensemble size on the surface.

The ordered Pd<sub>3</sub>Bi showed negligible MOR activity at room temperature, whereas the solid solution Pd<sub>3</sub>Bi demonstrated significant activity. Meanwhile, a partially ordered Pd<sub>3</sub>Bi alloy, exhibiting an ensemble size that lies between the two extremes, displayed an intermediate level of MOR activity, thereby reinforcing the direct correlation between the size of the ensemble and the catalytic reactivity of the material. This

peculiar contrast in reactivity between ordered Pd<sub>3</sub>Bi intermetallics and solid solution highlights the key role ensembles play in controlling the electrocatalytic behavior of a material. By addressing these challenges, we are establishing foundational knowledge that not only informs the design of high-performance catalysts but also supplies essential data for training machine learning/artificial intelligence algorithms for the predictive design of new electrocatalytic materials.<sup>38–40</sup> To date, the limited success of computational catalyst discovery may be from the difficulty in synthesizing materials with the precise atomic configuration used in calculations.<sup>39</sup> This approach opens new avenues for designing more efficient catalysts, demonstrating the potential to fine-tune catalytic activity by precisely manipulating the ensemble size of the active element.

## RESULTS AND DISCUSSION

**Structure and Characterization of Pd<sub>3</sub>Bi Alloys.** The Pd<sub>3</sub>Bi alloys were prepared by colloidal synthesis, more details can be found in the [Supporting Information](#). X-ray diffraction (XRD) was used to identify the crystal structures of the Pd<sub>3</sub>Bi nanoparticles (Figure 1c). Both ordered Pd<sub>3</sub>Bi and partially ordered Pd<sub>3</sub>Bi have an orthorhombic crystal structure and shared primary peaks at  $2\theta = 37.8, 41.1, 65^\circ$ . However, ordered Pd<sub>3</sub>Bi displayed sharper primary peaks and distinctive secondary peaks at  $2\theta = 36.1, 37.4, 71.1^\circ$  in comparison to the partially ordered sample. The solid-solution Pd<sub>3</sub>Bi sample, which is a metastable phase, possessed a face-centered cubic (FCC) crystal structure. This is evident from its XRD pattern, which is similar to elemental Pd but shifted to smaller angles from an increase in the lattice constant by Bi incorporation. The partially ordered Pd<sub>3</sub>Bi exhibited a small peak at  $2\theta = 45^\circ$  which indicates the coexistence of a solid solution Pd<sub>3</sub>Bi phase with the ordered orthorhombic Pd<sub>3</sub>Bi phase. Transmission electron microscopy (TEM) revealed that all the Pd<sub>3</sub>Bi materials consisted of isolated nanoparticles with mean diameters of ~8 to 9 nm (Figures S1–S3). High-angle annular dark-field scanning transmission electron microscopy (HAADF-STEM) was employed to investigate the extent of atomic ordering within the Pd<sub>3</sub>Bi phases (Figure 1d–f). Ordered Pd<sub>3</sub>Bi was composed of single-crystalline nanoparticles, as shown by a particle oriented along the [010] axis. The HAADF-STEM showed that the solid solution Pd<sub>3</sub>Bi nanoparticles consisted of single crystals which were oriented along the [110] axis. The partially ordered Pd<sub>3</sub>Bi samples contained both ordered (*Pmma* space group) and disordered (FCC) domains which coexisted within the crystals. This was evidenced by a particle displaying both an ordered domain along the [010] plane and a solid solution domain along the [011] plane. EDS elemental mapping and line scan analysis were also performed (Figures S4–S6). As shown from the elemental mapping, palladium and bismuth are well dispersed throughout the whole particle; meanwhile the line scan analysis revealed that the surface Pd/Bi elemental ratios across all samples was comparable. Additionally, the HAADF images and EDS mapping revealed no significant differences between the pristine samples and those subjected to catalysis, indicating the structural and compositional stability of the materials under the catalytic testing conditions used in this study (Figures 1 and S4–S9).

X-ray photoelectron spectroscopy (XPS) was used to determine the composition and chemical state of Pd and Bi in the Pd<sub>3</sub>Bi alloys by evaluating the Pd 3d and Bi 4f regions

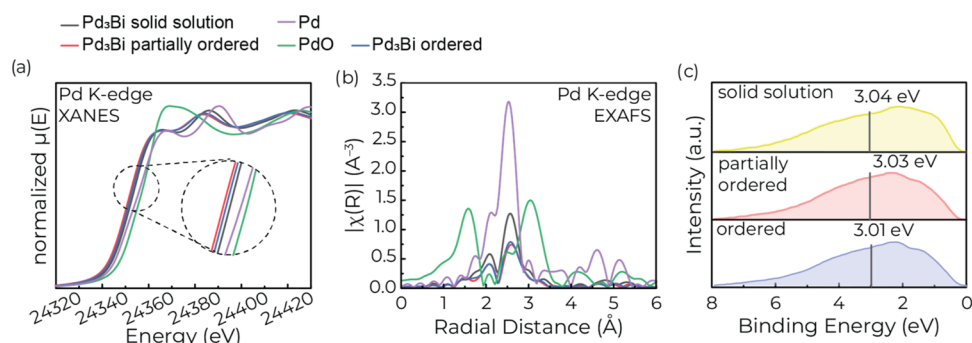


**Figure 2.** Ex situ X-ray spectroscopy of Pd<sub>3</sub>Bi alloys. (a) X-ray absorption near edge structure (XANES) spectra for Pd<sub>3</sub>Bi alloys, Pd and PdO to evaluate the oxidation state and electronic structure of the catalysts. The inset shows a zoom in of the edge region of the XANES spectra. (b) Extended X-ray absorption fine structure (EXAFS) spectra to evaluate the coordination environment of the Nearest neighbors of Pd in Pd<sub>3</sub>Bi alloys, Pd, and PdO. (c) X-ray photoelectron spectroscopy (XPS) valence band spectra of the Pd<sub>3</sub>Bi alloys. The gray vertical lines designate the valence band center ( $\epsilon_d$ ). The Fermi level is at 0 eV.

(Figure S10). XPS survey scans revealed that the atomic ratios of the materials were  $\sim 3$  Pd/1 Bi for all alloys, which agreed with the inductively coupled plasma mass spectrometry (ICP-MS) results (Figure S10 and Table S1).

The electronic structure and coordination environment of the Pd<sub>3</sub>Bi alloys were assessed using X-ray adsorption near-edge spectroscopy (XANES) and extended X-ray absorption fine structure (EXAFS) (Figures 2a,b and S11–S13).<sup>41</sup> Small shifts in the edge position of the XANES spectrum were observed revealing slight variations in the unoccupied density of states and corresponding changes to the local electronic environment of Pd (Figure 2a). Such subtleties suggest that the Pd<sub>3</sub>Bi phases have broadly similar electronic structures and are all metallic. A Fourier transform of the EXAFS oscillations of the Pd K-edge was performed to determine the local structure of Pd in the Pd<sub>3</sub>Bi alloys. The EXAFS analysis revealed an elongation in the bond distance within Pd's first coordination shell for all Pd<sub>3</sub>Bi phases, indicative of lattice expansion due to Bi incorporation. Specifically, the Pd–Pd bond lengths were observed to be  $2.79 \text{ \AA} \pm .01 \text{ \AA}$  (where  $\pm$  indicates the error of the measurement) for solid solution Pd<sub>3</sub>Bi,  $2.80 \text{ \AA} \pm .01 \text{ \AA}$  for the partially ordered Pd<sub>3</sub>Bi, and  $2.81 \text{ \AA} \pm .02$  for the ordered Pd<sub>3</sub>Bi, while the Pd–Bi distances were  $2.77 \text{ \AA} \pm .03 \text{ \AA}$ ,  $2.80 \text{ \AA} \pm .03 \text{ \AA}$ , and  $2.79 \text{ \AA} \pm .04 \text{ \AA}$  nm, respectively (Figure 2b and Table S2). The subtle changes in the XANES spectrum are likely from these minor alterations in Pd's bond length, although the overall impact on the electronic structure between the alloys remains small.

EXAFS analysis showed a decrease in the average Pd–Pd coordination number from solid solution Pd<sub>3</sub>Bi to partially ordered Pd<sub>3</sub>Bi to ordered Pd<sub>3</sub>Bi (i.e., in the direction of increasing atomic ordering). However, the absolute value of the coordination number (CN) are smaller than expected on the ordered and partially ordered materials because of destructive interference in the scattering path which causes an underestimation (Table S1).<sup>42</sup> Despite this limitation, valuable insights into the degree of mixing can be derived by comparing the ratios of Pd–Pd CN to Pd–Bi CN. For ordered Pd<sub>3</sub>Bi, this ratio was approximately 2, consistent with the ideal structure of orthorhombic Pd<sub>3</sub>Bi crystals, indicating a high degree of order. In contrast, the ratio was closer to 3 for the solid solution and partially ordered Pd<sub>3</sub>Bi, suggesting significant atomic mixing or a high density of defects.

XPS valence band spectroscopy was performed to determine the valence band center (i.e., the d-band center) of the Pd<sub>3</sub>Bi

alloys.<sup>43</sup> The d-band center was at  $3.04 \pm 0.01$  eV for solid-solution Pd<sub>3</sub>Bi,  $3.01 \pm 0.01$  eV for ordered Pd<sub>3</sub>Bi, and  $3.03 \pm 0.01$  eV for partially ordered Pd<sub>3</sub>Bi indicating that all the alloys showed a similar electronic structure. The observed shifts in the valence-band center are relatively minor, with a maximum variation of only 0.03 eV. In contrast, literature on other alloy systems typically reports valence band center shifts greater than 0.2 eV when the composition is varied to the extent that the ensemble sizes are substantially modified.<sup>29,44,45</sup> Taken together, we conclude that changes to the electronic structure is minor, and the key alterations in the material are likely driven by the size of Pd ensembles on the surface, which varies with the degree of atomic ordering within the Pd<sub>3</sub>Bi alloys.

An electrochemical reaction occurs at the surface of a material, so the geometry of active sites on the surface of the crystal is one of the primary parameters that effects electrochemical reactivity. Due to changes in the first coordination shell of Pd between the ordered and solid solution alloy (Figure 1a,b), we expect the ensemble size on the surface of ordered Pd<sub>3</sub>Bi to be smaller. The surface energies of various facets for ordered Pd<sub>3</sub>Bi were computed, revealing that the (100), (101), (111), and (110) facets have the lowest surface energy (Figure 3a). The ordered Pd<sub>3</sub>Bi does not exhibit a specific geometric shape, suggesting that a combination of these low-index facets are likely expressed on the surface. The Pd ensemble sizes for ordered Pd<sub>3</sub>Bi crystals are as follows: 5 and 4 for the (100) facet, 4 and 1 for the (110) facet, 5 and 3 for the (111) facet, and 5 for the (101) facet (Figure 3b). Solid solution Pd<sub>3</sub>Bi particles exhibit a nonspecific shape, suggesting the expression of a combination of the lowest energy facets in an FCC structure: (111), (110), and (100).<sup>46</sup> The ensemble size for an FCC crystal is 6 for (111), 6 for (101), and 5 for the (110) facets (Figure 3c). However, considering the material composition is 75% Pd, the average Pd ensemble size would be  $5.25 \pm 0.75$  for (111),  $5.25 \pm 0.75$  for (101), and  $3.75 \pm 1.25$  for the (110) facets (where the  $\pm$  represents the maximum and minimum value of the Pd ensembles). The Pd ensemble size varies depending on the statistical distribution of atoms, ranging from less than 5 atoms to up to 6 atoms for the (111) and (110) facets. This variability reflects the complexity of the atomic arrangement for the solid solution because the material is a statistically random structure. Nevertheless, this data suggests that the Pd–Pd ensemble size on ordered Pd<sub>3</sub>Bi is smaller than the solid solution Pd<sub>3</sub>Bi. Specifically, ordered Pd<sub>3</sub>Bi intermetallics

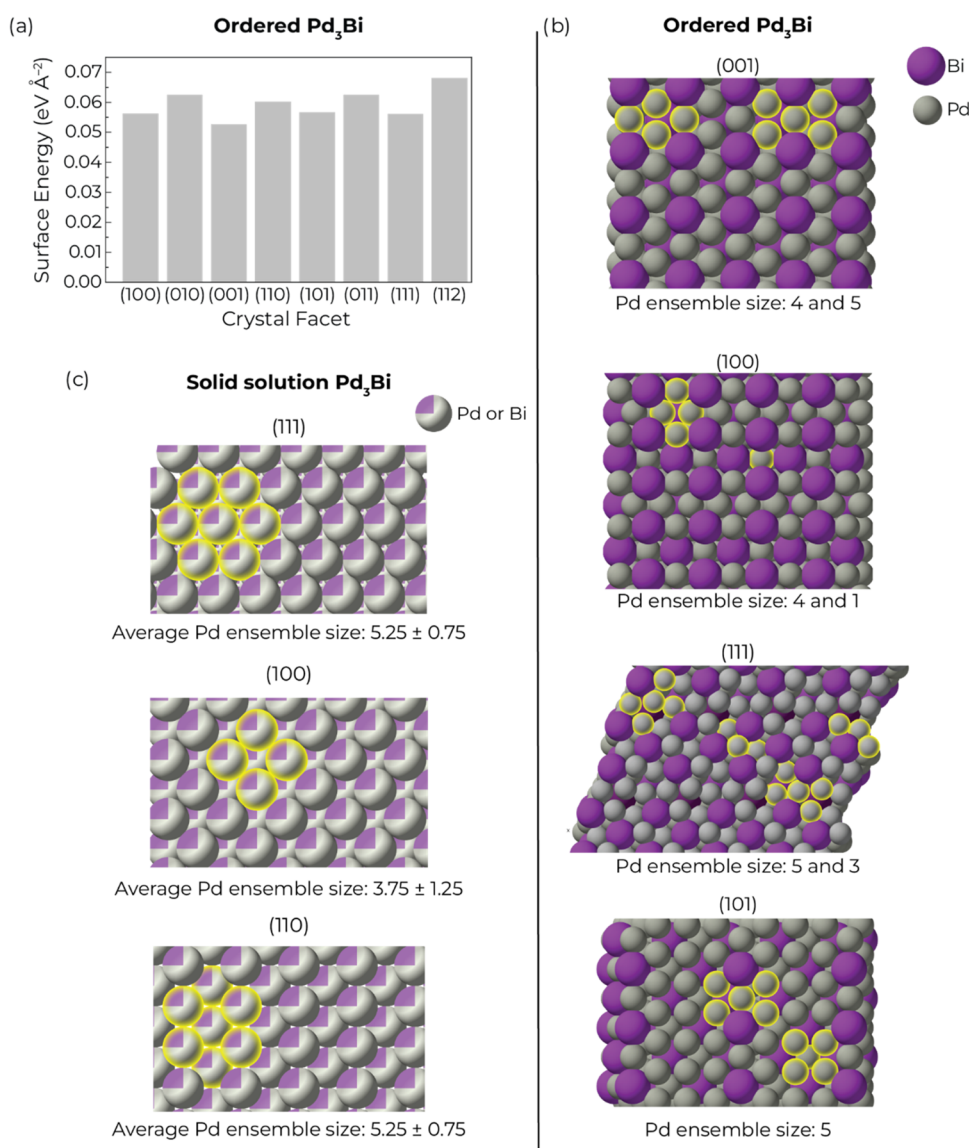


**Figure 3.** (a) Surface energy of various low-index facets of ordered Pd<sub>3</sub>Bi. Images showing the structure of the low energy facets of (b) ordered Pd<sub>3</sub>Bi, and (c) solid solution Pd<sub>3</sub>Bi. The yellow circles highlight the different geometric ensembles present on each facet. It is worth noting that one of the atoms highlighted in yellow on the (100) facet of solid solution Pd<sub>3</sub>Bi is buried beneath the four highlighted atoms. The average Pd ensemble size for the solid solution materials is provided, with the  $\pm$  values representing the maximum and minimum sizes of the Pd ensembles. The solid solution Pd<sub>3</sub>Bi is statistical random arrangement of Pd and Bi in the lattice, in which 75% of the occupied sites are Pd and 25% of the occupied sites are Bi.

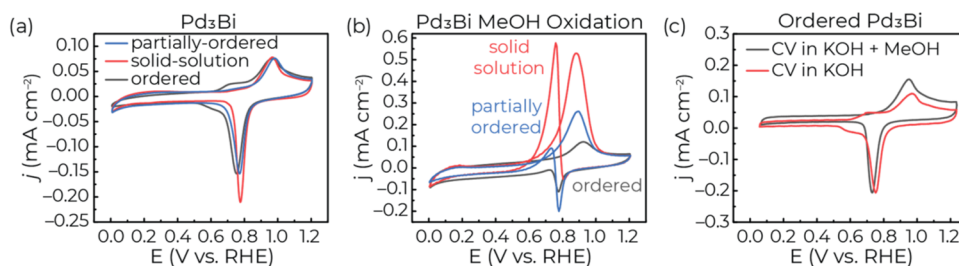


**Figure 4.** Cyclic voltammograms (CVs) of Pd<sub>3</sub>Bi alloys. (a) CVs of partially ordered Pd<sub>3</sub>Bi, ordered Pd<sub>3</sub>Bi, and solid solution Pd<sub>3</sub>Bi in N<sub>2</sub>-saturated 0.1 mol L<sup>-1</sup> KOH. (b) CVs of the same Pd<sub>3</sub>Bi materials in N<sub>2</sub>-saturated 0.1 mol L<sup>-1</sup> KOH + 0.5 mol L<sup>-1</sup> methanol. (c) CV of ordered Pd<sub>3</sub>Bi in 0.1 mol L<sup>-1</sup> KOH with and without 0.5 mol L<sup>-1</sup> methanol. All samples were measured on a rotating disc electrode at 20 mV s<sup>-1</sup> sweep rate and 900 rpm (94.25 rad s<sup>-1</sup>) rotation rate.

form smaller Pd ensembles (1, 3, 4, and 5 atoms across all low-energy facets), whereas solid solution Pd<sub>3</sub>Bi supports larger Pd

ensembles, with an average size of 5.25 atoms and up to 6 atoms on two of its lowest energy facets. Since the partially

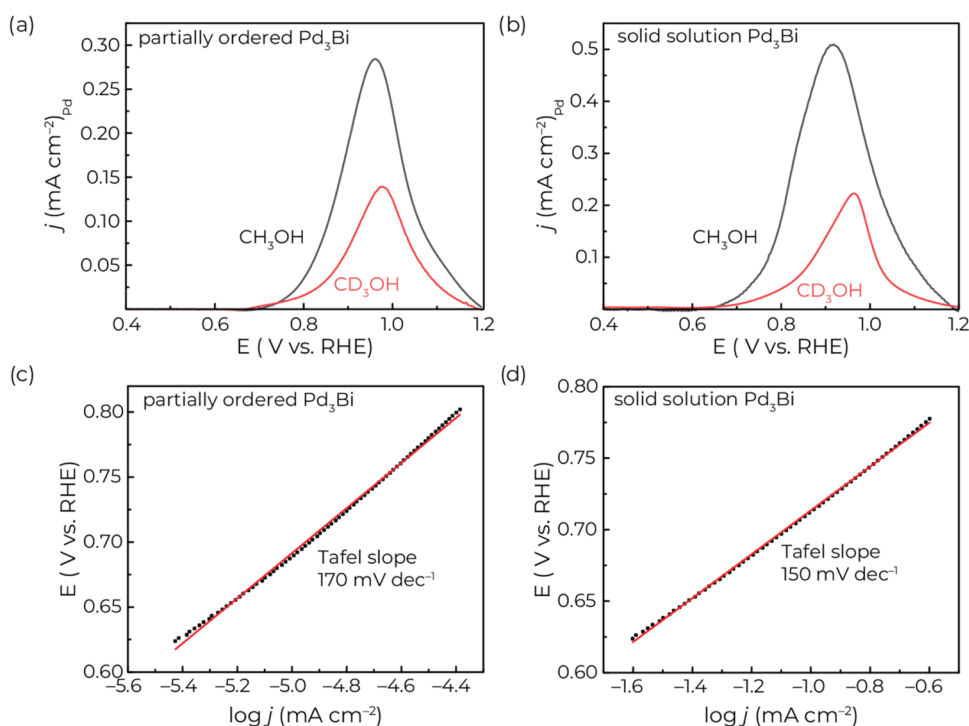


**Figure 5.** Oxidation of methanol and deuterated methanol with (a) partially ordered Pd<sub>3</sub>Bi, and (b) solid solution Pd<sub>3</sub>Bi. Tafel plot for methanol oxidation with (c) partially ordered Pd<sub>3</sub>Bi ( $R^2 = 0.998$ ), (d) solid solution Pd<sub>3</sub>Bi ( $R^2 = 0.999$ ). The measurements were performed on a rotating disk electrode at a rotation rate of 900 rpm in a solution containing 0.1 mol L<sup>-1</sup> KOH + 0.5 mol L<sup>-1</sup> methanol at room temperature with a voltage sweep rate of 20 mV s<sup>-1</sup>.

ordered material consists of a mixture of ordered and solid solution Pd<sub>3</sub>Bi, it should have a smaller fraction of Pd clusters of 5.25 atoms or greater compared to the solid solution alloy. Overall, the average size of the Pd ensembles on the surface follows this trend: ordered Pd<sub>3</sub>Bi < partially ordered Pd<sub>3</sub>Bi < solid solution Pd<sub>3</sub>Bi.

The voltammetric properties of the Pd<sub>3</sub>Bi alloys were assessed by performing cyclic voltammetry at a sweep rate of 20 mV s<sup>-1</sup> on a glassy carbon rotating disk electrode (RDE) in N<sub>2</sub>-saturated 0.1 mol L<sup>-1</sup> KOH. A graphite rod was used as the counter electrode in all electrochemical experiments. All data was referenced to the reversible hydrogen electrode (RHE) unless otherwise noted. The Pd<sub>3</sub>Bi alloys underwent voltage cycling until a stable voltammogram was obtained, typically achieving stabilization within 10 cycles or fewer. The stabilized voltammogram exhibited four distinct redox features (Figure 4a). The CV cycling cleaned the electrode surface and removed surface oxides before MOR measurements. In the anodic scan direction, redox waves were observed at 0.75 V, corresponding to hydroxyl adsorption, and 0.97 V, corresponding to the oxidation of Pd.<sup>47</sup> In the cathodic scan direction, we observed a wave at 0.77 V, corresponding to the reduction of oxidized Pd, and at 0.63 V, corresponding to hydroxyl desorption. Across all samples, the Pd-oxidation/reduction redox features were similar, indicating that this feature is nearly independent of the ensemble sizes examined in this study. Interestingly, the intensity of the hydroxyl sorption peaks was most prominent on the ordered Pd<sub>3</sub>Bi, suggesting a possible relationship with the Pd–Pd ensemble size.

The MOR was assessed by performing cyclic voltammetry (CV) in a solution containing 0.1 mol L<sup>-1</sup> KOH + 0.5 mol L<sup>-1</sup> MeOH while the RDE was rotated at 900 rpm. All Pd<sub>3</sub>Bi alloy samples were assessed using a uniform mass loading of 20 μg<sub>Pd</sub>

cm<sup>-2</sup>. The CVs were normalized by the electrochemically active surface area (ECSA), which was calculated from CO stripping measurements, taking into account only the palladium content. (Figure S14).<sup>48</sup> Solid solution Pd<sub>3</sub>Bi exhibited significant reactivity, characterized by the presence of two distinct oxidative waves at 0.9 and 0.75 V in the anodic and cathodic scan directions, respectively, with the peak current density reaching approximately 0.5 mA cm<sup>-2</sup> (Figure 4b and Figure S15). In contrast, ordered Pd<sub>3</sub>Bi displayed almost no reactivity, with the anodic and cathodic scans mostly overlapping the CVs obtained in the absence of MeOH (Figure 4c). Partially ordered Pd<sub>3</sub>Bi exhibited intermediate performance, featuring oxidative waves at the same voltages as the solid solution sample but with peak current densities of 0.25 and 0.1 mA cm<sub>Pd</sub><sup>-2</sup> for the anodic and cathodic scan directions, respectively. The observed trend in MeOH performance was found to correlate with increasing Pd ensemble size, following this order: ordered Pd<sub>3</sub>Bi < partially ordered Pd<sub>3</sub>Bi < solid solution Pd<sub>3</sub>Bi. Collectively, these findings suggest a direct impact of the average Pd–Pd CN (i.e. Pd ensemble) on the reactivity for methanol oxidation. It is worth noting that the overall similarity in the XANES edge features and valence band center across the materials confirms that the differences in catalytic activity are not from large changes in the electronic structure, but rather to variations in the size of the Pd ensembles.

**Mechanistic Insights of Pd<sub>3</sub>Bi during MOR.** To interrogate the mechanism of the methanol oxidation reaction (MOR) and the role of Pd ensembles in this process, we carried out electrode kinetic measurements. To investigate whether C–H bond breaking is a part of the rate-limiting step, we conducted the MOR using deuterated methanol (CD<sub>3</sub>OH) and compared the results with those obtained from regular

methanol ( $\text{CH}_3\text{OH}$ ) (Figure 5a,b). The rate of methanol oxidation was found to be approximately  $2.5\times$  lower for  $\text{CD}_3\text{OH}$  compared to  $\text{CH}_3\text{OH}$  for both the solid solution and partially ordered  $\text{Pd}_3\text{Bi}$  alloys. The Tafel slopes for the solid-solution and ordered samples were  $150\text{ mV dec}^{-1}$  and  $170\text{ mV dec}^{-1}$ , respectively (Figure 5c,d). These values are in close proximity to the standard Tafel slope of  $120\text{ mV dec}^{-1}$ , suggesting that the reaction rate is likely determined by a one-electron transfer in its initial step.<sup>49</sup> The observation of a kinetic isotope effect indicates that the cleavage of the methanol's C–H bond is the rate-determining step.<sup>50</sup> Taken together, the data collectively suggests that the cleavage of the C–H bond, occurring simultaneously with the first electron transfer from MeOH to the electrode, is the rate-determining step in the MOR on  $\text{Pd}_3\text{Bi}$  alloys.

We investigated the influence of ensemble size on the stabilization of the transition state during the oxidative C–H bond cleavage of methanol by determining the apparent activation energy ( $E_a$ ) of the reaction. The temperature dependence for the MOR was evaluated by collecting a series of linear sweep voltammograms between  $20$  and  $40\text{ }^\circ\text{C}$  at  $5\text{ }^\circ\text{C}$  intervals (Figure S16). As the temperature increased, the MeOH oxidation wave increased in magnitude across all alloys and the position of the peak shifted to more negative potentials. The ordered  $\text{Pd}_3\text{Bi}$  displayed virtually no activity at  $20\text{ }^\circ\text{C}$ , however at higher temperature the activity increased, and clear oxidation waves were observed. The  $E_a$  was determined by analyzing the slope of  $\ln(j)$  vs  $T^{-1}$  at a fixed overpotential since the kinetics of the reaction follow the Arrhenius equation

$$k = A e^{-E_a/RT}$$

where  $k$  is the rate constant of the reaction,  $A$  is the pre-exponential factor,  $E_a$  is the activation energy,  $R$  is the gas constant, and  $T$  is the temperature of the reaction. The rate constant is proportional to current density.

The  $E_a$  was found to systematically decrease with increasing degree of atomic-scale ordering across a broad range of potentials in the  $\text{Pd}_3\text{Bi}$  alloys, indicating a dependence on the Pd ensemble size within the alloys (Figure 6). Specifically, the solid solution  $\text{Pd}_3\text{Bi}$  sample displayed the lowest  $E_a$  of  $61.89\text{ kJ}$

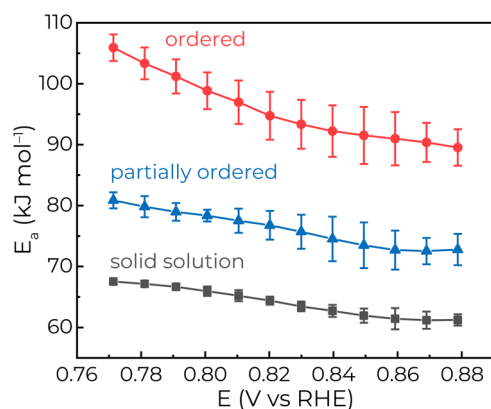


**Figure 6.** (a) Apparent activation energy ( $E_a$ ) for methanol electro-oxidation as a function of potential for the  $\text{Pd}_3\text{Bi}$  alloys taken in the anodic sweep direction. The data was collected in an electrolyte containing  $0.5\text{ mol L}^{-1}$  MeOH +  $0.1\text{ mol L}^{-1}$  KOH. The error bars represent the standard deviation derived from three repeated measurements, indicating the variability of the values.

$\text{mol}^{-1} \pm 1.17\text{ kJ mol}^{-1}$  at  $0.85\text{ V}$  vs RHE in the anodic scan direction. In contrast, the partially ordered  $\text{Pd}_3\text{Bi}$  had a slightly higher  $E_a$  of  $77.15\text{ kJ mol}^{-1} \pm 3.75\text{ kJ mol}^{-1}$ , while the ordered  $\text{Pd}_3\text{Bi}$  had the highest  $E_a$  at  $91.5\text{ kJ mol}^{-1} \pm 4.69\text{ kJ mol}^{-1}$  at  $0.85\text{ V}$  vs RHE in the anodic scan direction at that same voltage. This trend suggests a direct correlation between the size of Pd ensembles on the surface and the  $E_a$  for the reaction, where larger ensembles stabilize the transition state and lower the  $E_a$ .

Taking the electrode-kinetic measurements together, we observed that the efficiency of oxidative C–H bond breaking of MeOH during electro-oxidation is linked to the size of the Pd ensembles. The small Pd ensembles ( $\leq 5$  Pd atoms) in the ordered- $\text{Pd}_3\text{Bi}$  alloys are unable to effectively perform oxidative C–H bond cleavage as shown by the higher activation energies measured. Conversely, the larger Pd ensembles ( $> 5$  atoms) on the partially ordered and solid-solution  $\text{Pd}_3\text{Bi}$  alloys display lower activation energies for MeOH oxidation, suggesting they exhibit more efficient oxidative C–H bond cleavage. Our data indicates that the ensemble size is a critical determinant in the efficiency of oxidative C–H bond cleavage in the MOR, highlighting the importance of atomic arrangements (i.e., ensembles) within multicomponent materials in electrocatalysis.

## CONCLUSIONS

In this study, we developed a method that separates the influences of geometric effects from changes in electronic structure, thereby clarifying their contributions in electrocatalysis. By examining structurally distinct but compositionally identical  $\text{Pd}_3\text{Bi}$  polymorphs with similar electronic structure, we uncovered significant differences in catalytic behavior. Our findings revealed that the intermetallic  $\text{Pd}_3\text{Bi}$  exhibited negligible reactivity, while its solid-solution counterpart displayed pronounced activity for methanol electro-oxidation. This disparity in reactivity is linked to variations in the Pd ensemble sizes, with intermetallic  $\text{Pd}_3\text{Bi}$  having Pd ensembles  $\leq 5$  atoms, which has a high activation barrier for oxidative C–H bond cleavage. In contrast, the solid-solution  $\text{Pd}_3\text{Bi}$  has Pd ensembles with an average size of  $5.25 \pm 0.75$ , which lowered the activation barrier for oxidative C–H bond cleavage, effectively facilitating this reaction step. Notably, the partially ordered  $\text{Pd}_3\text{Bi}$  contained a smaller fraction of Pd ensembles which were larger than 5 atoms compared to the solid solution alloy, thus exhibiting moderate activity for methanol electro-oxidation. This study underscores the critical role of atomic arrangements within multicomponent materials in determining their electrocatalytic efficiency.

Our approach of modifying the arrangement of the same set of atoms by changing the alloy's polymorph can be used as a design strategy to interrogate the role of geometric effects (that is the ensemble size and configuration) in other multimetal alloys. However, it is crucial to note that the minor changes to electronic structure among different polymorphs is material-specific and must be assessed on a case-by-case basis.

## ASSOCIATED CONTENT

### Data Availability Statement

The data underpinning the conclusions drawn in this research are fully disclosed within the main text and its accompanying Supporting Information section. Furthermore, the corresponding author will provide data in response to well-founded inquiries.

**SI** Supporting Information

The Supporting Information is available free of charge at <https://pubs.acs.org/doi/10.1021/jacs.4c11753>.

Pd<sub>3</sub>Bi bulk static (CIF)

Comprehensive experimental details, including nanoparticle synthesis protocols, characterization techniques such as XRD, TEM, HAADF-STEM, XPS, XANES, and EXAFS, as well as electrochemical testing procedures. Additional data include size distributions of nanoparticles, elemental maps, line scans, ICP-MS analyses, cyclic voltammograms, and CO stripping voltammetry for ECSA determination. The document also contains quantitative data tables covering coordination numbers, bond distances, and calculated surface energies. Analyses related to methanol oxidation reaction (MOR) kinetics, temperature-dependent studies for activation energy determination, and isotope effects using CD<sub>3</sub>OH (PDF)

**AUTHOR INFORMATION****Corresponding Author**

**Anthony Shoji Hall** – Department of Materials Science and Engineering, Johns Hopkins University, Baltimore, Maryland 21218, United States; Present Address: Department of Materials Science and Engineering, University of Pennsylvania, Philadelphia, PA, 19104, United States; [orcid.org/0000-0003-4134-4160](https://orcid.org/0000-0003-4134-4160); Email: [shoji@jhu.edu](mailto:shoji@jhu.edu)

**Authors**

**Tianyao Gong** – Department of Materials Science and Engineering, Johns Hopkins University, Baltimore, Maryland 21218, United States; [orcid.org/0000-0002-9675-3853](https://orcid.org/0000-0002-9675-3853)

**Guotao Qiu** – Department of Materials Science and Engineering, Johns Hopkins University, Baltimore, Maryland 21218, United States

**Mo-Rigen He** – Department of Mechanical Engineering, Johns Hopkins University, Baltimore, Maryland 21218, United States

**Olga V. Safonova** – Paul Scherrer Institute, 5232 Villigen, Switzerland; [orcid.org/0000-0002-6772-1414](https://orcid.org/0000-0002-6772-1414)

**Wei-Chang Yang** – Material Measurement Laboratory, National Institute of Standards and Technology (NIST), Gaithersburg, Maryland 20899, United States; [orcid.org/0000-0002-7481-7916](https://orcid.org/0000-0002-7481-7916)

**David Raciti** – Material Measurement Laboratory, National Institute of Standards and Technology (NIST), Gaithersburg, Maryland 20899, United States; [orcid.org/0000-0002-9580-4524](https://orcid.org/0000-0002-9580-4524)

**Corey Oses** – Department of Materials Science and Engineering, Johns Hopkins University, Baltimore, Maryland 21218, United States

Complete contact information is available at: <https://pubs.acs.org/doi/10.1021/jacs.4c11753>

**Notes**

The authors declare no competing financial interest.

**ACKNOWLEDGMENTS**

A.S.H. acknowledges financial support from the National Science Foundation under award nos. CHE-2102648 and DMR-2047019. G.Q. and C.O. acknowledge support from the Ralph O'Connor Sustainable Energy Institute (ROSEI) at

JHU. C.O. also acknowledges support from the Advanced Research Projects Agency-Energy (ARPA-E) (DE-AR0001787) and the Advanced Research Computing at Hopkins (ARCH). Certain equipment, instruments, software or materials, commercial or noncommercial, are identified in this paper to specify the experimental procedure adequately. Such identification is not intended to imply recommendation or endorsement of any product or service by the National Institute of Standards and Technology, nor is it intended to imply that the materials or equipment identified are necessarily the best available for the purpose.

**REFERENCES**

- (1) Askins, E. J.; Zoric, M. R.; Li, M.; et al. Toward a mechanistic understanding of electrocatalytic nanocarbon. *Nat. Commun.* **2021**, *12*, No. 3288.
- (2) Verma, S.; Lu, S.; Kenis, P. J. A. Co-electrolysis of CO<sub>2</sub> and glycerol as a pathway to carbon chemicals with improved technoconomics due to low electricity consumption. *Nat. Energy* **2019**, *4*, 466–474.
- (3) Kibria, M. G.; Edwards, J. P.; Gabardo, C. M.; et al. Electrochemical CO<sub>2</sub> Reduction into Chemical Feedstocks: From Mechanistic Electrocatalysis Models to System Design. *Adv. Mater.* **2019**, *31*, No. 1807166.
- (4) Gong, T.; Alghamdi, H.; Raciti, D.; Hall, A. S. Improved Alkaline Hydrogen Oxidation on Strain-Modulated Pt Overlayers at Ordered Intermetallic Pt–Sb Cores. *ACS Energy Lett.* **2023**, *8*, 685–690.
- (5) Renner, J. N.; Greenlee, L. F.; Ayres, K. E.; Herring, A. M. Electrochemical Synthesis of Ammonia: A Low Pressure, Low Temperature Approach. *Interface Mag.* **2015**, *24*, No. 51.
- (6) Wu, Z.-Y.; Karamad, M.; Yong, X.; et al. Electrochemical ammonia synthesis via nitrate reduction on Fe single atom catalyst. *Nat. Commun.* **2021**, *12*, No. 2870.
- (7) Horiuti, I.; Polanyi, M. Exchange reactions of hydrogen on metallic catalysts. *Trans. Faraday Soc.* **1934**, *30*, 1164–1172.
- (8) Kwon, Y.; Birdja, Y.; Spanos, I.; Rodriguez, P.; Koper, M. T. M. Highly Selective Electro-Oxidation of Glycerol to Dihydroxyacetone on Platinum in the Presence of Bismuth. *ACS Catal.* **2012**, *2*, 759–764.
- (9) Furukawa, S.; Komatsu, T. Intermetallic Compounds: Promising Inorganic Materials for Well-Structured and Electronically Modified Reaction Environments for Efficient Catalysis. *ACS Catal.* **2017**, *7*, 735–765.
- (10) Hu, C.; Chen, Z.; Han, F.; Lin, Z.; Yang, X. Surface engineering of ultrasmall supported Pd<sub>x</sub>Bi nanoalloys with enhanced electrocatalytic activity for selective alcohol oxidation. *Chem. Commun.* **2019**, *55*, 13566–13569.
- (11) Yan, Y.; Du, J. S.; Gilroy, K. D.; et al. Intermetallic Nanocrystals: Syntheses and Catalytic Applications. *Adv. Mater.* **2017**, *29*, No. 1605997.
- (12) Yu, J.; Yu, S. W.; Qi, Z.; et al. Synthesis of PtSn<sub>4</sub> Intermetallic Nanodisks through a Galvanic Replacement Mechanism. *Chem. Mater.* **2022**, *34*, 6968–6976.
- (13) Kim, C.; Dionigi, F.; Beermann, V.; et al. Alloy Nanocatalysts for the Electrochemical Oxygen Reduction (ORR) and the Direct Electrochemical Carbon Dioxide Reduction Reaction (CO<sub>2</sub>RR). *Adv. Mater.* **2019**, *31*, No. 1805617.
- (14) Xiao, W.; Lei, W.; Wang, J.; et al. Tuning the electrocatalytic activity of Pt by structurally ordered PdFe/C for the hydrogen oxidation reaction in alkaline media. *J. Mater. Chem. A* **2018**, *6*, 11346–11352.
- (15) Schreier, M.; Kenis, P.; Che, F.; Hall, A. S. Trends in Electrocatalysis: The Microenvironment Moves to Center Stage. *ACS Energy Lett.* **2023**, *8*, 3935–3940.
- (16) Hammer, B.; Nørskov, J. K. Theoretical Surface Science and Catalysis—Calculations and Concepts. In *Advances in Catalysis*; Academic Press, 2000; Vol. 45, pp 71–129.

- (17) Cuesta, A. Atomic Ensemble Effects in Electrocatalysis: The Site-Knockout Strategy. *ChemPhysChem* **2011**, *12*, 2375–2385.
- (18) Foucher, A. C.; Rosen, D. J.; Yang, S.; et al. Stable and Efficient Ir Nanoshells for Oxygen Reduction and Evolution Reactions. *Chem. Mater.* **2023**, *35*, 4572–4580.
- (19) Sinfelt, J. H. *Bimetallic Catalysts: Discoveries, Concepts, and Applications*; Sinfelt, J. H., Ed.; Wiley: New York, 1983.
- (20) Sachtler, W. M. H.; Van Der Plank, P. The role of individual surface atoms in chemisorption and catalysis by nickel-copper alloys. *Surf. Sci.* **1969**, *18*, 62–79.
- (21) Du, B.; Tong, A. Coverage-Dependent Study of Pt Spontaneously Deposited onto Au and Ru Surfaces: Direct Experimental Evidence of the Ensemble Effect for Methanol Electro-Oxidation on Pt. *J. Phys. Chem. B* **2005**, *109*, 17775–17780.
- (22) Dasgupta, A.; He, H.; Gong, R.; et al. Atomic control of active-site ensembles in ordered alloys to enhance hydrogenation selectivity. *Nat. Chem.* **2022**, *14*, 523–529.
- (23) Pérez-Ramírez, J.; López, N. Strategies to break linear scaling relationships. *Nat. Catal.* **2019**, *2*, 971–976.
- (24) Maroun, F.; Ozanam, F.; Magnussen, O. M.; Behm, R. J. The Role of Atomic Ensembles in the Reactivity of Bimetallic Electrocatalysts. *Science* **2001**, *293*, 1811–1814.
- (25) Gao, F.; Goodman, D. W. Pd–Au bimetallic catalysts: understanding alloy effects from planar models and (supported) nanoparticles. *Chem. Soc. Rev.* **2012**, *41*, 8009–8020.
- (26) Li, H.; Shin, K.; Henkelman, G. Effects of ensembles, ligand, and strain on adsorbate binding to alloy surfaces. *J. Chem. Phys.* **2018**, *149*, No. 174705.
- (27) Garipey, Z.; Chen, G.; Xu, A.; et al. Machine learning assisted binary alloy catalyst design for the electroreduction of CO<sub>2</sub> to C<sub>2</sub> products. *Energy Adv.* **2023**, *2*, 410–419.
- (28) Kim, D.; Resasco, J.; Yu, Y.; Asiri, A. M.; Yang, P. Synergistic geometric and electronic effects for electrochemical reduction of carbon dioxide using gold–copper bimetallic nanoparticles. *Nat. Commun.* **2014**, *5*, No. 4948.
- (29) Tang, F.; Wang, L.; Dessie Walle, M.; Mustapha, A.; Liu, Y.-N. An alloy chemistry strategy to tailoring the d-band center of Ni by Cu for efficient and selective catalytic hydrogenation of furfural. *J. Catal.* **2020**, *383*, 172–180.
- (30) Friedrich, M.; Villaseca, S. A.; Szentmiklósi, L.; Teschner, D.; Armbrüster, M. Order-Induced Selectivity Increase of Cu<sub>60</sub>Pd<sub>40</sub> in the Semi-Hydrogenation of Acetylene. *Materials* **2013**, *6*, 2958–2977.
- (31) Abe, H.; Matsumoto, F.; Alden, L. R.; et al. Electrocatalytic Performance of Fuel Oxidation by Pt<sub>3</sub>Ti Nanoparticles. *J. Am. Chem. Soc.* **2008**, *130*, 5452–5458.
- (32) Gamler, J. T. L.; Ashberry, H. M.; Skrabalak, S. E.; Koczkur, K. M. Random Alloyed versus Intermetallic Nanoparticles: A Comparison of Electrocatalytic Performance. *Adv. Mater.* **2018**, *30*, No. 1801563.
- (33) Chen, H.; Nishijima, M.; Wang, G.; et al. The Ordered and Disordered Nano-Intermetallic AuCu/C Catalysts for the Oxygen Reduction Reaction: The Differences of the Electrochemical Performance. *J. Electrochem. Soc.* **2017**, *164*, No. F1654.
- (34) Zhang, J.; Zhang, L.; Cui, Z. Strategies to enhance the electrochemical performances of Pt-based intermetallic catalysts. *Chem. Commun.* **2021**, *57*, 11–26.
- (35) Chen, H.-S.; Benedetti, T. M.; Lian, J.; et al. Role of the Secondary Metal in Ordered and Disordered Pt–M Intermetallic Nanoparticles: An Example of Pt<sub>3</sub>Sn Nanocubes for the Electrocatalytic Methanol Oxidation. *ACS Catal.* **2021**, *11*, 2235–2243.
- (36) Zalineaeva, A.; Serov, A.; Padilla, M.; et al. Self-Supported PdxBi Catalysts for the Electrooxidation of Glycerol in Alkaline Media. *J. Am. Chem. Soc.* **2014**, *136*, 3937–3945.
- (37) Schubert, K.; Bhan, S.; Biswas, T. K.; Frank, K.; Panday, P. K. Einige Strukturdaten metallischer Phasen. *Naturwissenschaften* **1968**, *55*, 542–543.
- (38) Akbashev, A. R. Electrocatalysis Goes Nuts. *ACS Catal.* **2022**, *12*, 4296–4301.
- (39) Chen, B. W. J.; Xu, L.; Mavrikakis, M. Computational Methods in Heterogeneous Catalysis. *Chem. Rev.* **2021**, *121*, 1007–1048.
- (40) Chen, Y.; Miao, R. K.; Yu, C.; et al. Catalyst design for electrochemical CO<sub>2</sub> reduction to ethylene. *Matter* **2024**, *7*, 25–37.
- (41) Wang, J.; Hsu, C. S.; Wu, T. S.; et al. In situ X-ray spectroscopies beyond conventional X-ray absorption spectroscopy on deciphering dynamic configuration of electrocatalysts. *Nat. Commun.* **2023**, *14*, No. 6576.
- (42) Hausmann, J. N.; Ashton, M.; Mebs, S.; et al. Intermetallic Cobalt Indium Nanoparticles as Oxygen Evolution Reaction Precatalyst: A Non-Leaching p-Block Element. *Small* **2024**, *20*, No. 2309749, DOI: 10.1002/smll.202309749.
- (43) Hofmann, T.; Yu, T. H.; Folse, M.; et al. Using Photoelectron Spectroscopy and Quantum Mechanics to Determine d-Band Energies of Metals for Catalytic Applications. *J. Phys. Chem. C* **2012**, *116*, 24016–24026.
- (44) Tang, W.; Zhang, L.; Henkelman, G. Catalytic Activity of Pd/Cu Random Alloy Nanoparticles for Oxygen Reduction. *J. Phys. Chem. Lett.* **2011**, *2*, 1328–1331.
- (45) Wu, X.; Chen, F.; Zhang, N.; et al. Activity Trends of Binary Silver Alloy Nanocatalysts for Oxygen Reduction Reaction in Alkaline Media. *Small* **2017**, *13*, No. 1603387.
- (46) Wen, Y.-N.; Zhang, J.-M. Surface energy calculation of the fcc metals by using the MAEAM. *Solid State Commun.* **2007**, *144*, 163–167.
- (47) Burke, L. D.; Casey, J. K. An Examination of the Electrochemical Behavior of Palladium in Base. *J. Electrochem. Soc.* **1993**, *140*, No. 1292.
- (48) Raciti, D.; Schwarz, K. A.; Vinson, J.; Stafford, G. R. Compressive Stress and Charge Redistribution during CO Adsorption onto Pt. *J. Phys. Chem. C* **2022**, *126*, 4446–4457.
- (49) Fletcher, S. Tafel slopes from first principles. *J. Solid State Electrochem.* **2009**, *13*, 537–549.
- (50) Hou, G.; Parrondo, J.; Ramani, V.; Prakash, J. Kinetic and Mechanistic Investigation of Methanol Oxidation on a Smooth Polycrystalline Pt Surface. *J. Electrochem. Soc.* **2014**, *161*, No. F252.



CAS BIOFINDER DISCOVERY PLATFORM™

**ELIMINATE DATA SILOS. FIND WHAT YOU NEED, WHEN YOU NEED IT.**

A single platform for relevant, high-quality biological and toxicology research

**Streamline your R&D**

CAS  
A Division of the American Chemical Society